LETTERS
https://doi.org/10.1038/s41563-019-0346-z

nature materials

Atomic and electronic reconstruction at the van der Waals interface in twisted bilayer graphene

Hyobin Yoo[1], Rebecca Engelke[1], Stephen Carr[1], Shiang Fang[1], Kuan Zhang[2], Paul Cazeaux[3], Suk Hyun Sung[4], Robert Hovden[4], Adam W. Tsen[5], Takashi Taniguchi[6], Kenji Watanabe[6], Gyu-Chul Yi[7], Miyoung Kim[8], Mitchell Luskin[9], Ellad B. Tadmor[2], Efthimios Kaxiras[1,10] and Philip Kim[1]*

Control of the interlayer twist angle in two-dimensional van der Waals (vdW) heterostructures enables one to engineer a quasiperiodic moiré superlattice of tunable length scale[1–8]. In twisted bilayer graphene, the simple moiré superlattice band description suggests that the electronic bandwidth can be tuned to be comparable to the vdW interlayer interaction at a 'magic angle'[9], exhibiting strongly correlated behaviour. However, the vdW interlayer interaction can also cause significant structural reconstruction at the interface by favouring interlayer commensurability, which competes with the intralayer lattice distortion[10–16]. Here we report atomic-scale reconstruction in twisted bilayer graphene and its effect on the electronic structure. We find a gradual transition from an incommensurate moiré structure to an array of commensurate domains with soliton boundaries as we decrease the twist angle across the characteristic crossover angle, $\theta_c \approx 1°$. In the solitonic regime ($\theta < \theta_c$) where the atomic and electronic reconstruction become significant, a simple moiré band description breaks down and the secondary Dirac bands appear. On applying a transverse electric field, we observe electronic transport along the network of one-dimensional topological channels that surround the alternating triangular gapped domains. Atomic and electronic reconstruction at the vdW interface provide a new pathway to engineer the system with continuous tunability.

In van der Waals (vdW) heteroepitaxy where atomic-scale reconstruction is generally assumed to be absent[17], a small rigid rotation of the vdW layers relative to each other results in a moiré pattern, whose long-wavelength periodicity is determined by the twist angle. However, the interplay between the vdW interaction energy and the elastic energy at the interface can cause atomic reconstruction, leading to intriguing structures. For unreconstructed twisted bilayer graphene (TBG), the atomic registry varies continuously across the moiré period between three distinct types of symmetric stacking configuration: energetically favourable AB and BA Bernal stacking and unfavourable AA stacking (Fig. 1a). This quasiperiodic moiré superlattice, associated with the incommensurability of the twisted layers, modifies the band structure significantly. In the small-twist regime, low-energy flat bands appear at a series of magic angles ($\theta_{magic} \leq 1.1°$) where the diverging density of states (DOS) and vanishing Fermi velocity, associated with strong electronic correlation, are predicted[9]. A recent experiment demonstrated the presence of the first magic angle near ~1.1° where a Mott insulator and unconventional superconductivity were observed[7,8]. The TBG moiré band calculation, however, assumes a rigid rotation of layers ignoring atomic-scale reconstruction. Despite the weak nature of the vdW interaction and the absence of dangling bonds, recent experimental works on similar material systems suggest that there is substantial lattice reconstruction at vdW interfaces, especially at a small twist angle close to global commensuration between two adjacent layers[10,11,18]. Atomic-scale reconstruction at vdW interfaces induces significant changes in lattice symmetry and electronic structure[10–16]. In TBG, the interfacial reconstruction is expected to occur by rotating the lattice locally (marked by arrows in Fig. 1a) to form an array of domains with Bernal stacking configurations similar to the schematic diagram shown in Fig. 1b.

Here we employ transmission electron microscopy (TEM) combined with electron transport measurements and first-principle calculations to investigate the effect of lattice reconstruction in TBGs with a small twist angle θ. We fabricate TBG samples with the twist angle in the range of $0 < \theta < 4°$ by employing the experimental technique reported in previous studies[5–8] (see Supplementary Section 1 for fabrication details). Figure 1c shows a false-colour optical microscopy image of TBG covered with multilayer hexagonal boron nitride (hBN) on a thin SiN membrane for TEM study. Micromechanical manipulation combined with a microscopic probe allows us to engineer and study TBG with less than 10% variation in length scale (domain size) for more than 10^3 moiré unit cells with a domain size up to ~200 nm.

Formation of the commensurate domains via reconstruction can be probed by mapping the stacking order of TBG using TEM dark-field imaging. This experimental technique employs an aperture to filter a specific Bragg peak g on the diffraction plane, providing a spatial map of the stacking order (see Methods for details). Figure 1d shows the dark-field image ($\boldsymbol{g} = 10\bar{1}0$) obtained from a TBG sample with a series of different twist angles. The $\boldsymbol{g} = 10\bar{1}0$ dark-field image obtained from a TBG sample with 0.1° twist shows a tessellation of triangular domains that alternate with mirrored

[1]Department of Physics, Harvard University, Cambridge, MA, USA. [2]Aerospace Engineering and Mechanics, University of Minnesota, Minneapolis, MN, USA. [3]Department of Mathematics, University of Kansas, Lawrence, KS, USA. [4]Department of Materials Science and Engineering, University of Michigan, Ann Arbor, MI, USA. [5]Institute for Quantum Computing and Department of Chemistry, University of Waterloo, Waterloo, Ontario, Canada. [6]National Institute for Materials Science, Ibaraki, Japan. [7]Department of Physics and Astronomy, Seoul National University, Seoul, Republic of Korea. [8]Department of Materials Science and Engineering, Seoul National University, Seoul, Republic of Korea. [9]School of Mathematics, University of Minnesota, Minneapolis, MN, USA. [10]John A. Paulson School of Engineering and Applied Sciences, Harvard University, Cambridge, MA, USA. *e-mail: pkim@physics.harvard.edu

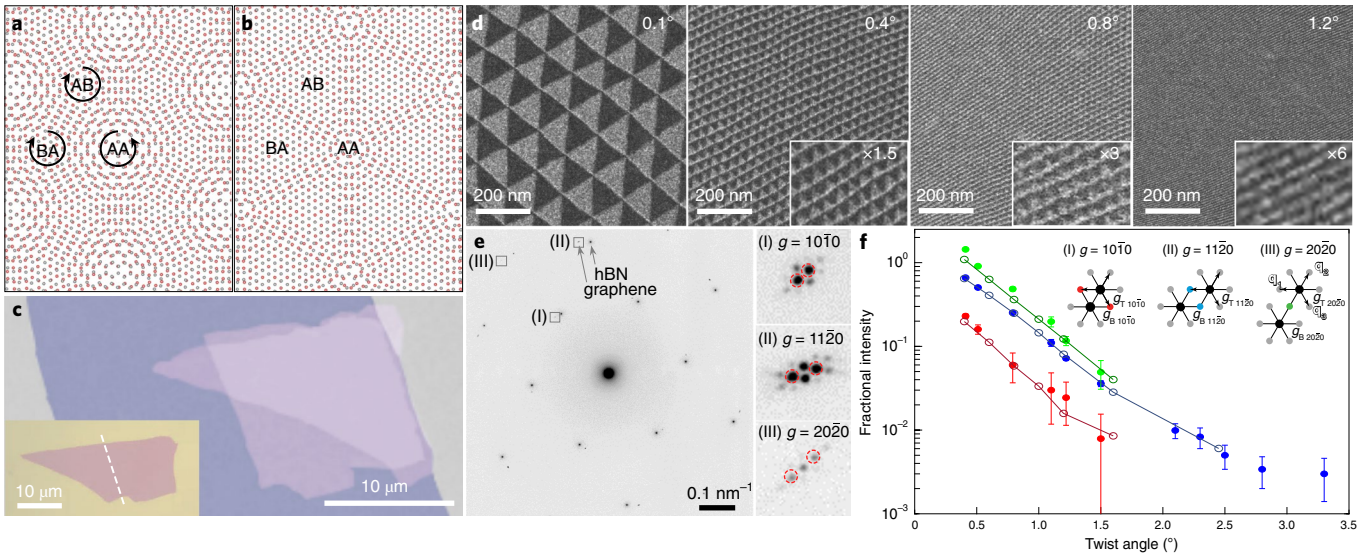

Fig. 1 | Atomic-scale reconstruction in TBG with a controlled twist angle. a,**b**, Schematic diagrams of TBG before (**a**) and after (**b**) the atomic reconstruction. Periodic rotational modulation of the lattice is represented with the arrows in **a**. **c**, A false-colour optical microscope image of artificial bilayer graphene with a controlled twist angle covered with an hBN layer. The purple and blue coloured regions correspond to graphene and hBN, respectively. The inset shows an optical microscope image of the original graphene layer employed to fabricate the TBG in the main panel. The graphene was torn along the dashed line indicated in the inset. **d**, TEM dark-field images obtained by selecting the graphene diffraction peak (g = 10$\bar{1}$0) in TBG with a series of controlled twist angles. The alternating contrast of AB/BA domains is associated with the antisymmetric shift of lattice period in AB and BA domains. **e**, The SAED pattern of TBG covered with an hBN layer (<5 nm) with a twist angle of 0.4°. Diffraction peaks originating from graphene and hBN are marked with arrows. Each of the graphene peaks marked with a black square and roman numerals is magnified and represented on the right side to show details of the Bragg and satellite peaks. The red dashed circles indicate the Bragg peaks with the Miller indices shown in the images. **f**, Plot of fractional intensity (I_{sat}/I_{Bra}) as a function of twist angle of the TBG. The filled circles with error bars were obtained from experimental SAED patterns, and the open circles and line fits were obtained from simulated SAED patterns[16]. The error bars show the uncertainty in measured intensity due to background fluctuations. The red, blue and green plots correspond to the satellite peaks marked with red, blue and green filled circles schematically represented in the inset. Bragg peaks of graphene ($g_{T(B)\ 10\bar{1}0}$, $g_{T(B)\ 11\bar{2}0}$, $g_{T(B)\ 20\bar{2}0}$) are represented as black filled circles, and satellite peaks are represented as red, blue, green and grey circles. The subscripts T and B indicate the top and bottom layers, respectively. Three basis vectors ($\mathbf{q}_1$, $\mathbf{q}_2$, $\mathbf{q}_3$) for the lattice modulation index satellite peaks.

symmetry (AB/BA), matching the periodicity of the moiré pattern. The periodic array of domain structures separated by sharp mirror boundaries indicates an interfacial atomic reconstruction in TBG that is schematically represented in Fig. 1a,b (see Supplementary Section 2 for details). The domain contrast observed in 0.1° is similar to the previous reports on AB/BA domains formed in chemically vapour-deposited bilayer graphene (BLG)[18–20]. As we increase the twist angle, however, we can clearly observe that the triangular domain contrast is weakened and becomes close to one-directional fringes (insets of Fig. 1d), which typically appear in the simple rotational moiré structure without reconstruction[21]. This trend suggests that the reconstruction strength, and thus the degree of commensurability within the domains, increases with decreasing θ (see Supplementary Sections 4 and 5).

We study the reconstruction in TBG as a function of θ by investigating selected-area electron diffraction (SAED) in a systematic manner. Figure 1e shows a representative SAED pattern obtained from TBG with $\theta = 0.4°$. In this SAED image, we identify two sets of diffraction peaks with sixfold rotation symmetry. The brighter set corresponds to Bragg peaks from a thicker hBN layer, and the weaker set of Bragg peaks corresponds to the TBG. A close inspection of the TBG Bragg peaks (right panels of Fig. 1e) reveals that the two main Bragg peaks from the top and bottom graphene layers, marked with red dashed circles, are surrounded by satellite peaks. These satellite peaks are associated with a periodic modulation of much larger scale than that of the atomic lattice. Here, the periodicity and strength of the lattice modulation can be quantified by the position and intensity of the satellite peaks (Supplementary Sections 4 and 5). SAED patterns obtained from a series of different twist angles (Supplementary Section 4) show that the configurational arrangement of the satellite peaks is not changed as a function of twist angle: all of the satellite peak positions in reference to the adjacent Bragg peaks indicated with the wavevectors $\mathbf{q}_j$ are equal to the moiré wavevectors defined by the vector difference between the reciprocal lattice vectors $\mathbf{g}_{T(B)}$ for the top and bottom layer (the inset of Fig. 1f). This relation indicates that the periodic lattice modulation at the interface is commensurate with the moiré superlattice that is determined by the twist angle θ.

Quantitative analysis of structural reconstruction can be performed by studying the intensity of a satellite peak (I_{sat}) and the adjacent Bragg peak (I_{Bra}). We note that TBG is an extremely thin system where we can obtain quantitative details of atomic structures via investigating the diffraction intensity under the kinematic approximation (see Supplementary Section 3). Figure 1f shows experimentally measured I_{sat}/I_{Bra} for the first-, second- and third-order Bragg peaks measured in 11 different samples in the range of $0° < \theta < 4°$. For $\theta > 4°$, I_{sat} is under the experimental detection limit, indicating that no appreciable reconstruction occurs in this large-θ limit (see Supplementary Section 4). We find that I_{sat}/I_{Bra} decreases rapidly as θ increases, following an empirical relation, $I_{sat}/I_{Bra} \sim e^{-\alpha\theta}$ with the constant $\alpha \approx 2.75 \pm 0.3$ (in the unit of inverse degree) obtained from the linear slope presented in Fig. 1f. We note that α describes how fast the reconstruction strength decreases as θ increases and thus is related to the measure of interlayer interaction of the system, which plays a key role to determine both structural reconstruction and electronic band structure modification.

We study the diffraction peak intensity further to obtain insight into the atomic-scale registry and reconstruction as a function of θ. Although the diffraction peak intensity contains quantitative details of atomic reconstruction (see Supplementary Section 5 for details), achieving complete structural information directly from the diffraction pattern is not trivial due to the lost phase information in the SAED. Here we performed a finite-element method (FEM) simulation to model the structural reconstruction and compare it with the experimental observation. Using the atomic coordinates of the reconstructed TBG obtained from the FEM model, the SAED pattern can be computed (Supplementary Fig. 4b) where I_{sat}/I_{Bra} shows a close match with the experimental data exhibiting similar exponential decaying behaviour (open circles in Fig. 1f). We note that the FEM model exhibits a crossover in structural reconstruction across the characteristic angle, $\theta_c \cong 1^\circ$ (ref. [16]). For $\theta < \theta_c$, nearly commensurate domains are formed, characterized by an atomic registry close to Bernal stacking and separated by sharp boundaries. The width of the domain boundaries is constant in this regime ($\theta < \theta_c$) associated with the formation of solitonic features regardless of the twist angle. For $\theta > \theta_c \cong 1^\circ$, the atomic registry in the domains starts deviating from Bernal stacking in a large portion making the transition from one domain to the other rather gradual. The crossover in structural reconstruction occurs when the moiré length scale becomes comparable to the domain boundary width[15]. Therefore, the balance between the interlayer energy and the intralayer elastic energy forms domains with reduced commensurability, suppressing the formation of solitons.

The electronic structure of the TBG samples can be probed by electrical transport measurement. We measure the electrical conductance G in the TBG devices as a function of the charge carrier density n of the TBG samples tuned by the gate voltage. From the side-peak position, we can identify the domain size and the corresponding twist angle (see Supplementary Section 6). We find that the estimated twist angle is consistent with the targeted twist angle within experimental precision ($\pm 0.3^\circ$). Figure 2a,c (top panels) shows the experimentally measured conductance G of TBG at different temperatures T as a function of n/n_0, where $n_0 = 1/A$ and A is the area of the moiré unit cell. Here we show the results obtained from two representative twist angles, $\theta \approx 1.1^\circ$ and 0.5°, respectively, corresponding to the first and second magic angle predicted in the TBG moiré structure without reconstruction[9]. Near the first magic angle, $G(n = \pm 4n_0)$ exhibits a well-developed zero at low temperatures, corresponding to the single-particle gap due to the band hybridization, which is consistent with the previous report[5]. We also observe the correlated Mott gap developing at $n = \pm 2n_0$, corresponding to the half-filled band as shown in the previous study[8]. As T increases, the minimum of $G(n = \pm 4n_0)$ and $G(n = \pm 2n_0)$ exhibits an activating behaviour (Supplementary Section 6) with the activation energy corresponding to 27 meV (18 meV) and 0.30 meV (0.22 meV), for the electron (hole) side, respectively, indicating that the corresponding energy gaps are developing at these fillings. Near the second magic angle, however, $G(n)$ exhibit non-zero minima without an activation behaviour, at the single-particle band filling $n/n_0 = \pm 4, \pm 8$, suggesting the absence of the energy gap.

To understand the experimentally observed charge transport, we calculate the electronic band structures for the reconstructed TBG structure obtained from the FEM model discussed above. We present the single-particle band structure (Fig. 2b) and corresponding DOS (Fig. 2a, middle and bottom panels) for both unreconstructed and reconstructed configurations in TBG with $\theta = 1.1^\circ$. We note that the reconstructed TBG exhibits sizable gaps of 32 meV and 26 meV for electrons and holes, respectively, which exhibit better agreement with experimentally observed gaps than those from the unreconstructed TBG where no or much smaller gap are shown (Fig. 2b). We also note that the overall DOS is reduced in the reconstructed band compared to unreconstructed ones as the bands themselves have larger dispersion. Structural reconstruction occurring at the twist regime above or close to the crossover angle ($\theta \geq \theta_c$) seems to change the details of the band structure such as the single-particle gap size and band dispersion. Nevertheless, the essential physics related to the magic angle (that is, the singular development of the DOS peaks due to the flat band condition) remains qualitatively intact.

At the twist angle regime below the crossover angle ($\theta < \theta_c$), however, the electronic band structure of reconstructed TBG differs significantly from that of unreconstructed TBG. To study the reconstruction effect below the crossover angle regime, we choose the representative twist angle close to the theoretically predicted second magic angle, $\theta \approx 0.5^\circ$. The DOS for the unreconstructued system near 0.5° has many sharp features (Fig. 2c, middle) due to the erratic nature of the unreconstructed band structure (Fig. 2d, left). Those sharp features are not stable under small changes in twist angle, implying that any experimental measurement of the low-energy transport would be extremely sensitive to the small change in the twist angle. In contrast, the DOS for the reconstructed TBG near 0.5° exhibits sharp features at $n/n_0 = 0$, ± 4 and ± 8 with their minima close to zero, which correspond to the Dirac-like band crossing shown in the reconstructed band structure (Fig. 2d, right). We note that this observation is generally reproducible with small changes in θ (Fig. 2c, bottom) near 0.5°. Experimental observation agrees well with the reconstructed band structure at $\theta \cong 0.5^\circ$. It is clear that the conductance $G(n)$ measured for TBG with $\theta = 0.47^\circ$ shows minima at $n/n_0 = 0$, ± 4 and ± 8 without gap opening, suggesting the appearance of the secondary Dirac spectrum. Furthermore, the low-field Hall effect measurement shows Hall sign reversal across $n/n_0 = 0$, ± 4 and ± 8 (see Supplementary Section 6 for details), supporting our conclusion. It is also noted that the DOS features at $n/n_0 = \pm 4$ are lifted from zero and become less sharp for certain angles. We associate these features with the non-degenerate dispersion near the higher-order Dirac point that is sensitive to the details of how the reconstructed lattice is described in the computation. Moreover, the reconstructed TBG bands exhibit larger dispersion than unreconstructed ones. The more than an order of magnitude suppression in the DOS peaks in this small-θ limit compared to those in the first magic angle near 1.1° suggests that no significant correlated electronic behaviours occur in this regime.

Although the correlated electronic behaviour seems to be suppressed in the small-twist-angle regime ($\theta < \theta_c$), the enhanced atomic and electronic reconstruction create a network of chiral 1D propagation channels. Under a transverse electric field, the nearly commensurate AB and BA domains are gapped out, leaving topologically protected 1D conduction channels along their boundaries[22–29]. Figure 3a–c shows the longitudinal resistance R_{xx} as a function of top- (V_{top}) and bottom- (V_{bot}) gate voltages for three BLG samples: (i) Bernal-stacked BLG ($\theta = 0$), (ii) a large-angle TBG ($\theta \cong 2.8^\circ > \theta_c$) and (iii) small-angle TBG ($\theta = 0.47^\circ < \theta_c$). For a fixed value of V_{top}, R_{xx} (V_{bot}) displays a maximum value at the charge neutrality point (CNP). The location of these maxima appears as a diagonal line in the $V_{top}-V_{bot}$ plane, where the average transverse electric displacement field $D = \frac{C_{top}V_{top} - C_{bot}V_{bot}}{2} - D_0$ can be tuned. Here, C_{top} (C_{bot}) is the top (bottom)-gate capacitance and D_0 is a small residual displacement field.

Figure 3d shows the displacement-tunable resistance R_{xx} along the CNP line, $R(D)$, normalized by the resistance at the global CNP ($D = 0$), R_0. For $\theta = 0$ (that is, a Bernal-stacked BLG), R/R_0 increases rapidly as $|D|$ increases due to the gap opening at the CNP by breaking inversion symmetry[30–32] (inset of Fig. 3a). For large-angle TBG ($\theta \cong 2.8^\circ$), however, R/R_0 decreases as $|D|$ increases. The electronic band of this large-angle TBG can be described by two Dirac cones displaced in reciprocal space with negligibly small interlayer coupling (inset of Fig. 3b)[33,34]. Thus, the weakly coupled layers are doped with an equal amount but opposite sign of carriers as $|D|$ increases, making both layers less resistive. In contrast, the electron transport

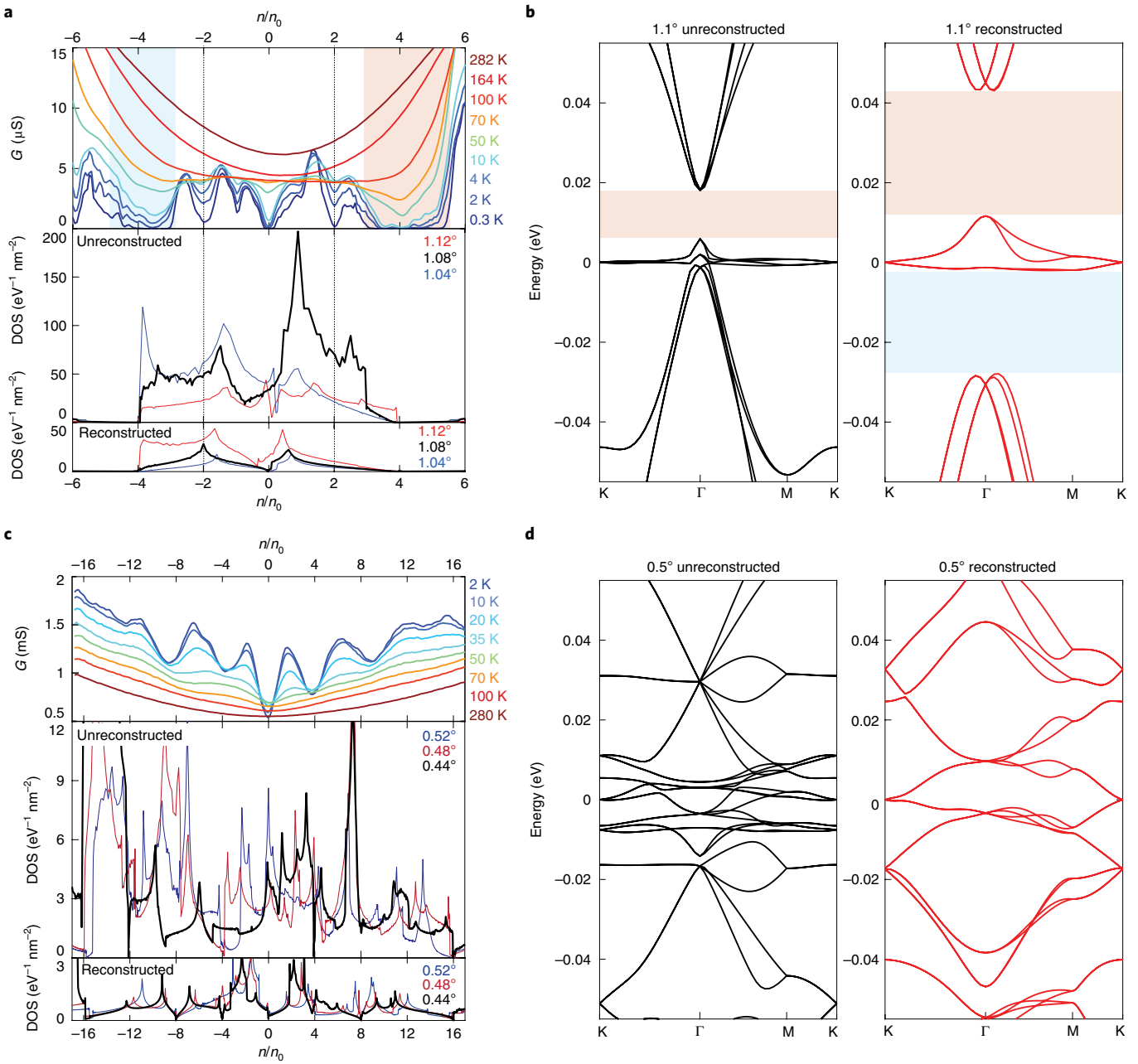

Fig. 2 | Electronic reconstruction in TBG. a, Temperature-dependent conductance G measured from a TBG device with $\theta = 1.1°$ from 0.3 K to 282 K (top). Calculated DOS without (middle) and with (bottom) reconstruction for three angles near 1.1° in units of density normalized by 1 electron per moiré supercell (n_0). **b**, Band structures for the TBG ($\theta = 1.1°$) without (left) and with (right) reconstruction. Reconstruction changes the details of the band structure such as single-particle gap size, bandwidth and overall DOS. However, the essential physics of the correlated behaviour stays the same. **c**, Temperature-dependent conductance G measured from a TBG device with $\theta = 0.47°$ from 2 K to 280 K (top). Calculated DOS without (middle) and with (bottom) reconstruction for three angles near 0.5°. **d**, Band structures for TBG ($\theta = 0.5°$) without (left) and with (right) reconstruction. Here reconstruction changes the band structures significantly and explains the single-particle features of gate-dependent conductance.

behaviours observed in the small-angle TBG ($\theta = 0.47°$) (iii) are distinctly different from the Bernal-stacked BLG (i) and large-angle TBG (ii) discussed above. The effect of the domain structures on transport properties becomes evident when the transverse displacement field is applied to form two topologically distinct insulating states in AB and BA domains, creating a network of 1D topological channels along the domain boundaries (inset of Fig. 3c)[22–29]. Here, each 1D conducting channel, represented as a simple resistor in the schematic diagram, carries quantum resistance $R_q = h/4e^2$. Experimentally, $R(D)$ measured from the small-angle TBG devices ($\theta < \theta_c$) increases and saturates as one applies higher $|D|$ (inset of Fig. 3d). This observation is consistent with the picture where the current is directed to the 1D network of conducting channels as the AB/BA domains are gapped at higher $|D|$[26]. The saturation values of $R(D)$ are of similar order of magnitude to R_q, as expected from a simple network of R_q assuming incoherent mixing of currents at vertices (see Supplementary Section 6 for details). We also note that the formation of 1D conducting channels can be related to the locally varying pseudo-magnetic field developed by lattice strain[14]. Coherent electronic transport through the network of such 1D channels

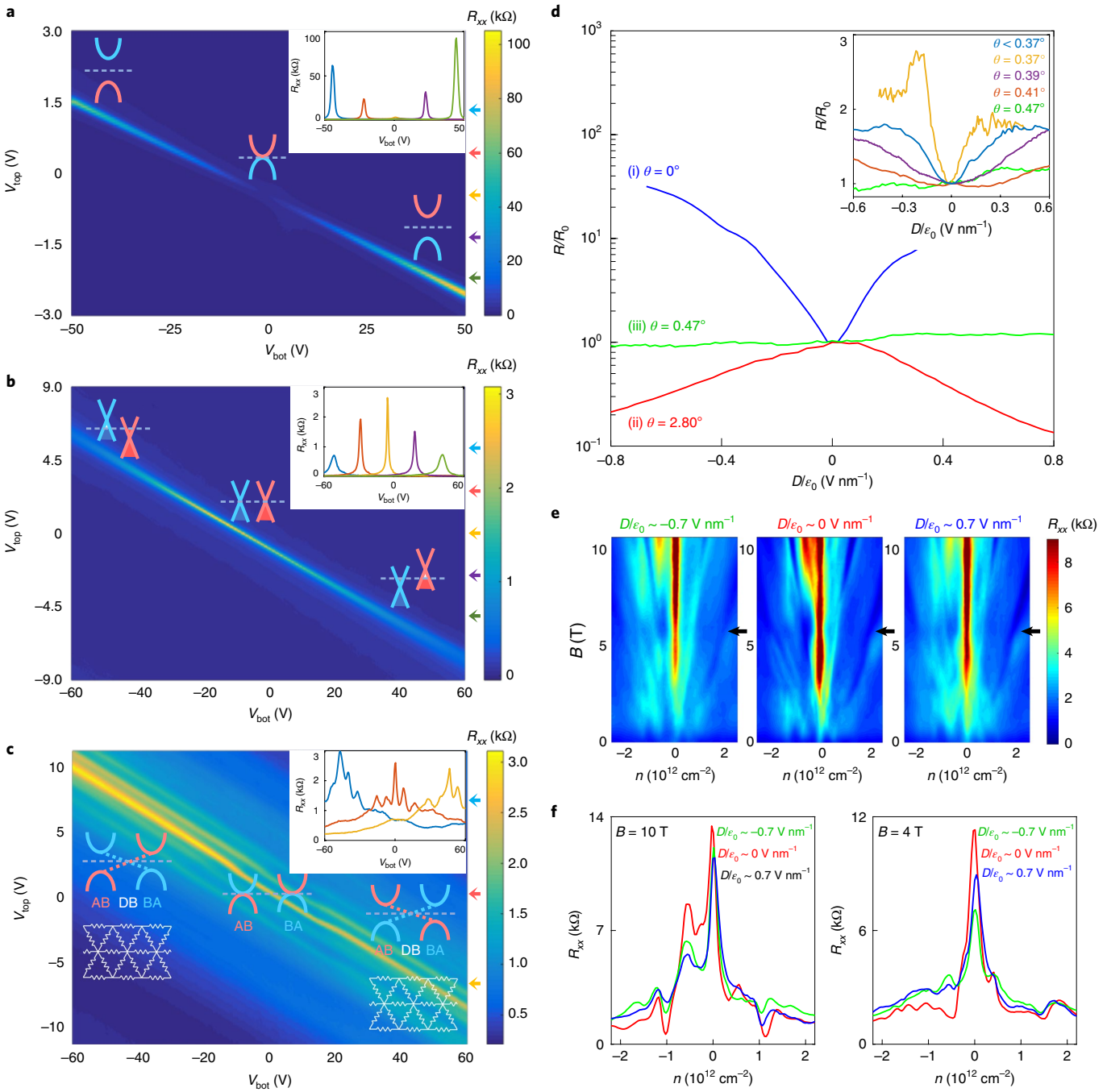

Fig. 3 | Transport properties of BLG with a controlled twist angle. a–c, The top- and bottom-gate dependence of the longitudinal resistance R_{xx} in Bernal-stacked BLG (**a**), large-angle TBG (2.8°) (**b**) and small-angle TBG (0.47°) (**c**). The insets in the top right corner show several line cuts at fixed top-gate voltages marked with coloured arrows on the right side of the main panels. Schematic band structures in the inset show how the band structures change as a function of the perpendicular electric displacement field, D. The schematic diagram of the triangular network of resistors in **c** represents the current paths generated along the domain boundaries obtained by gapping out AB and BA domains with transverse electric field. DB denotes the domain boundaries. **d**, Normalized Dirac peak resistances as a function of transverse displacement field obtained from **a–c**. The inset shows a linear-scale plot of normalized Dirac peak resistances as a function of the electric displacement field, D, for small-angle TBG devices. **e**, Displacement field-dependent Landau fan diagrams showing longitudinal resistance R_{xx}. The fan diagrams shown in the left, middle and right panels were obtained at the displacement field $D/\varepsilon_0 \approx -0.7$, 0 and 0.7 V nm^{-1}, respectively. **f**, Displacement field-dependent longitudinal resistance R_{xx} acquired at constant $B = 10$ T (left) and 4 T (right). Green, red and blue curves correspond to the displacement field $D/\varepsilon_0 \approx -0.7$, 0 and 0.7 V nm^{-1}, respectively. All the transport measurements were performed at 1.7 K.

in TBG was probed previously using Aharonov–Bohm oscillations with the aid of a cavity effect in a local gated region of the TBG samples[29]. Our experimental observation above further suggests that the electronic transport through the 1D topological channels can be extended to the entire area of mesoscale TBG device.

With the 1D topological channels formed across the entire device, we can probe the length scale of the 1D channel network and its topologically protected transport mode. We investigate magnetotransport in the small-angle TBG ($\theta = 0.47°$) with an applied magnetic field B perpendicular to the plane. Figure 3e shows R_{xx} as

a function of B and n at fixed D. We observe well-developed Landau fans originating from the main Dirac peaks at the CNP as well as other Landau fans from the side peaks, indicating development of the fractal spectrum known as Hofstadter's butterfly[3,4,35]. Multiple quantum Hall features fan out from two sets of side peaks, creating periodic quantum Hall features when the magnetic flux per supercell ϕ becomes integer multiples of the magnetic flux quantum $\phi_0 = h/e$. The most salient feature in these fan diagrams is the horizontal features appearing in all three different displacement field conditions ($D/\varepsilon_0 \approx -0.7$, 0 and $0.7\,\mathrm{V\,nm^{-1}}$) at $B = 5.4\,\mathrm{T}$ (marked with black arrows in Fig. 3e). $B = 5.4\,\mathrm{T}$ is the magnetic field corresponding to $\frac{\phi}{\phi_0} = 1$, where the magnetic flux $\phi = \mathrm{BA}$ with the area of the moiré unit cell yields $\theta = 0.47°$. This estimated value of θ from the fractal spectrum is consistent with the estimation from the side-peak positions (see Supplementary Section 6). Interestingly, we notice that the observed Hofstadter features become substantially weaker as $|D|$ increases (see Fig. 3f). The suppression of the quantum Hall features at high displacement field suggests the decrease of Landau gaps in the Hofstadter fractal energy spectrum. We thus attribute this change in the fan diagram to the transition of electronic transport from the 2D to 1D network mode with increasing $|D|$, confining the carriers to the topologically protected boundaries of gapped AB/BA domains in structurally reconstructed TBG. Together with our experimental finding of the crossover between the soliton and moiré regime, the appearance of these topological modes can be further utilized in engineering vdW epitaxy of 2D materials.

Online content

Any methods, additional references, Nature Research reporting summaries, source data, statements of data availability and associated accession codes are available at https://doi.org/10.1038/s41563-019-0346-z.

Received: 10 April 2018; Accepted: 15 March 2019;
Published online: 15 April 2019

References

1. Li, G. et al. Observation of Van Hove singularities in twisted graphene layers. *Nat. Phys.* **6**, 109–113 (2010).
2. Ponomarenko, L. et al. Cloning of Dirac fermions in graphene superlattices. *Nature* **497**, 594–597 (2013).
3. Dean, C. R. et al. Hofstadter's butterfly and the fractal quantum Hall effect in moiré superlattices. *Nature* **497**, 598–602 (2013).
4. Hunt, B. et al. Massive Dirac fermions and Hofstadter butterfly in a van der Waals heterostructure. *Science* **340**, 1427–1430 (2013).
5. Cao, Y. et al. Superlattice-induced insulating states and valley-protected orbits in twisted bilayer graphene. *Phys. Rev. Lett.* **117**, 116804 (2016).
6. Kim, K. et al. Tunable moiré bands and strong correlations in small-twist-angle bilayer graphene. *Proc. Natl Acad. Sci. USA* **114**, 3364–3369 (2017).
7. Cao, Y. et al. Unconventional superconductivity in magic-angle graphene superlattices. *Nature* **556**, 43–50 (2018).
8. Cao, Y. et al. Correlated insulator behaviour at half-filling in magic-angle graphene superlattices. *Nature* **556**, 80–84 (2018).
9. Bistritzer, R. & MacDonald, A. H. Moiré bands in twisted double-layer graphene. *Proc. Natl Acad. Sci. USA* **108**, 12233–12237 (2011).
10. Woods, C. et al. Commensurate–incommensurate transition in graphene on hexagonal boron nitride. *Nat. Phys.* **10**, 451–456 (2014).
11. Kim, N. Y. et al. Evidence of local commensurate state with lattice match of graphene on hexagonal boron nitride. *ACS Nano* **11**, 7084–7090 (2017).
12. Van Wijk, M., Schuring, A., Katsnelson, M. & Fasolino, A. Relaxation of moiré patterns for slightly misaligned identical lattices: graphene on graphite. *2D Materials* **2**, 034010 (2015).
13. Dai, S., Xiang, Y. & Srolovitz, D. J. Twisted bilayer graphene: moiré with a twist. *Nano Lett.* **16**, 5923–5927 (2016).
14. Nam, N. N. T. & Koshino, M. Lattice relaxation and energy band modulation in twisted bilayer graphene. *Phys. Rev. B* **96**, 075311 (2017).
15. Gargiulo, F. & Yazyev, O. V. Structural and electronic transformation in low-angle twisted bilayer graphene. *2D Materials* **5**, 015019 (2018).
16. Zhang, K. & Tadmor, E. B. Structural and electron diffraction scaling of twisted graphene bilayers. *J. Mech. Phys. Solids* **112**, 225–238 (2018).
17. Koma, A. Van der Waals epitaxy—a new epitaxial growth method for a highly lattice-mismatched system. *Thin Solid Films* **216**, 72–76 (1992).
18. Alden, J. S. et al. Strain solitons and topological defects in bilayer graphene. *Proc. Natl Acad. Sci. USA* **110**, 11256–11260 (2013).
19. Lin, J. et al. AC/AB stacking boundaries in bilayer graphene. *Nano Lett.* **13**, 3262–3268 (2013).
20. Butz, B. et al. Dislocations in bilayer graphene. *Nature* **505**, 533–537 (2014).
21. Yuk, J. M. et al. Superstructural defects and superlattice domains in stacked graphene. *Carbon* **80**, 755–761 (2014).
22. Zhang, F., MacDonald, A. H. & Mele, E. J. Valley Chern numbers and boundary modes in gapped bilayer graphene. *Proc. Natl Acad. Sci. USA* **110**, 10546–10551 (2013).
23. Vaezi, A., Liang, Y., Ngai, D. H., Yang, L. & Kim, E.-A. Topological edge states at a tilt boundary in gated multilayer graphene. *Phys. Rev. X* **3**, 021018 (2013).
24. Ju, L. et al. Topological valley transport at bilayer graphene domain walls. *Nature* **520**, 650–655 (2015).
25. Huang, S. et al. Topologically protected helical states in minimally twisted bilayer graphene. *Phys. Rev. Lett.* **121**, 037702 (2018).
26. San-Jose, P. & Prada, E. Helical networks in twisted bilayer graphene under interlayer bias. *Phys. Rev. B* **88**, 121408 (2013).
27. Anđelković, M., Covaci, L. & Peeters, F. M. DC conductivity of twisted bilayer graphene: Angle-dependent transport properties and effects of disorder. *Phys. Rev. Mater.* **2**, 034004 (2018).
28. Li, J. et al. Gate-controlled topological conducting channels in bilayer graphene. *Nat. Nanotechnol.* **11**, 1060–1065 (2016).
29. Rickhaus, P. et al. Transport through a network of topological channels in twisted bilayer graphene. *Nano Lett.* **18**, 6725–6730 (2018).
30. McCann, E. Asymmetry gap in the electronic band structure of bilayer graphene. *Phys. Rev. B* **74**, 161403 (2006).
31. Castro, E. V. et al. Biased bilayer graphene: semiconductor with a gap tunable by the electric field effect. *Phys. Rev. Lett.* **99**, 216802 (2007).
32. Oostinga, J. B., Heersche, H. B., Liu, X., Morpurgo, A. F. & Vandersypen, L. M. Gate-induced insulating state in bilayer graphene devices. *Nat. Mater.* **7**, 151–157 (2008).
33. Dos Santos, J. L., Peres, N. & Neto, A. C. Graphene bilayer with a twist: Electronic structure. *Phys. Rev. Lett.* **99**, 256802 (2007).
34. Sanchez-Yamagishi, J. D. et al. Quantum Hall effect, screening, and layer-polarized insulating states in twisted bilayer graphene. *Phys. Rev. Lett.* **108**, 076601 (2012).
35. Hofstadter, D. R. Energy levels and wave functions of Bloch electrons in rational and irrational magnetic fields. *Phys. Rev. B* **14**, 2239–2249 (1976).

Acknowledgements

We thank Y. Cao and P. Jarillo-Herrero for important discussions. The authors acknowledge the support of the Army Research Office (W911NF-14-1-0247) under the MURI programme. Part of the TEM analysis was supported by the Global Research Laboratory Program (2015K1A1A2033332) through the National Research Foundation of Korea (NRF). P.K. acknowledges partial support from the Gordon and Betty Moore Foundation's EPiQS Initiative through grant GBMF4543 and the Lloyd Foundation. R.E. acknowledges support from the National Science Foundation Graduate Research Fellowship under grant no. DGE1745303. P.C. acknowledges support from the National Science Foundation under grant no. DMS-1819220. K.W. and T.T. acknowledge support from the Elemental Strategy Initiative conducted by the MEXT, Japan and the CREST (JPMJCR15F3), JST. Nanofabrication was performed at the Center for Nanoscale Systems at Harvard, supported in part by NSF NNIN award ECS-00335765.

Author contributions

H.Y. and P.K. conceived the experiments. H.Y. and R.E. performed the experiments and analysed the data. S.C., S.F. and E.K. performed the density functional theory calculation. K.Z. and E.B.T. conceived and performed the theoretical and FEM analyses. P.C. and M.L. performed mathematical modelling analysis. S.H.S., R.H., A.W.T., G.-C.Y. and M.K. performed TEM data analysis. K.W. and T.T. provided bulk hBN crystals. H.Y., R.E. and P.K. wrote the manuscript. All authors contributed to the overall scientific interpretation and edited the manuscript.

Competing interests

The authors declare no competing interests.

Additional information

Supplementary information is available for this paper at https://doi.org/10.1038/s41563-019-0346-z.

Reprints and permissions information is available at www.nature.com/reprints.

Correspondence and requests for materials should be addressed to P.K.

Publisher's note: Springer Nature remains neutral with regard to jurisdictional claims in published maps and institutional affiliations.

Methods

TEM experiment. TBG was fabricated by tearing single-layer graphene into two pieces and engaging them together with a controlled twist angle using a top BN layer (see Supplementary Section 1 for details). Using the straight edges of the flakes, we intentionally misaligned the top BN layer with the graphene to resolve the diffraction pattern of graphene clearly without overlap with that of BN and also to avoid possible reconstruction between graphene and BN that is expected to occur when they are closely aligned[10,11]. To detect weak satellite peaks in the diffraction pattern clearly and improve the dark-field image contrast, it is preferable to have the thickness of the top BN layer and underlying SiN membrane as thin as possible. In this work, ~5-nm-thick BN and less than 10-nm-thick amorphous SiN membrane were used. An 80 kV field-emission TEM (Jeol 2010F) equipped with a Gatan One View camera was used for SAED and dark-field imaging. AB/BA domain contrast was obtained by taking a $g = 10\bar{1}0$ image with the specimen tilted off the zone axis as demonstrated in a previous report[36].

FEM simulation. Simulations were performed using a novel continuum–atomistic FEM method for 2D layered heterostructures[16]. A subdivision FEM formulation is used, which provides a smooth parameterization with square integrable curvature. Each layer is treated as a separate mesh that interacts with its neighbour through an interlayer energy density that is integrated across the domain using an efficient discrete–continuum scheme[37]. The mechanical response within a graphene layer is described by a nonlinear elastic model, which consists of a Saint Venant–Kirchhoff membrane term and a Helfrich bending term[38,39]. Non-bonded interactions between the layers are described using a Kolmogorov–Crespi model, which accounts for registry effects at the interface[40]. A stable equilibrium configuration is obtained by minimizing the total energy of the entire assembly using L-BFGS (see Supplementary Section 4 for details).

Density functional theory calculation. The electronic structure of TBG was modelled using previously obtained ab initio tight-binding parameters[41,42]. The band structures were computed with a standard supercell tight-binding Hamiltonian while the DOS used an ab initio continuum model[43]. An FEM[44] was used on a 60 × 60 k-point grid to generate the DOS profiles. Reconstructions were obtained with a continuum model[45] based on the parameters reported previously[46]. The momentum-dependent strain field and interlayer coupling terms were defined in a large enough range of k to capture the details of the reconstructed lattice. This strain field correction becomes more significant as one approaches the solitonic regime ($\theta < \theta_c$) where the reconstructed lattice cannot be captured with only a few Fourier components.

Transport measurement. For electrical transport measurement, encapsulated TBG devices with dual gates were fabricated on SiO_2/Si substrates. The typical thickness of the top and bottom BN was 15–40 nm. We used electron beam lithography to define the top gate, Hall bar and contact patterns. The top gate was made with Cr/Au (5 nm/70 nm) using BN as the gate insulator, and then the flakes were etched to define a Hall bar pattern using a reactive ion etcher with a mixture of CHF_3, Ar and O_2. Finally, 1D side contact to the graphene was made with Cr/Pd/Au (2 nm/10 nm/70 nm)[47]. Heavily doped Si substrate with 285-nm-thick SiO_2 was used as the bottom gate. The transport measurement was performed in a four-probe configuration using a lock-in amplifier at 17.7 Hz with a biasing current of 10–30 nA. A TBG device with $\theta = 1.1°$ was measured in a two-probe configuration using a lock-in amplifier at 17.7 Hz with a bias voltage of 200 μV in a ^{3}He cryostat.

Data availability

The data that support the findings of this study are available from the corresponding author upon reasonable request.

References

36. Brown, L. et al. Twinning and twisting of tri- and bilayer graphene. *Nano Lett.* **12**, 1609–1615 (2012).
37. Zhang, K. & Tadmor, E. B. Energy and moiré patterns in 2D bilayers in translation and rotation: A study using an efficient discrete-continuum interlayer potential. *Extreme Mech. Lett.* **14**, 16–22 (2017).
38. Zhang, K. & Arroyo, M. Understanding and strain-engineering wrinkle networks in supported graphene through simulations. *J. Mech. Phys. Solids* **72**, 61–74 (2014).
39. Zhang, K. & Arroyo, M. Coexistence of wrinkles and blisters in supported graphene. *Extreme Mech. Lett.* **14**, 23–30 (2017).
40. Kolmogorov, A. N. & Crespi, V. H. Registry-dependent interlayer potential for graphitic systems. *Phys. Rev. B* **71**, 235415 (2005).
41. Fang, S. & Kaxiras, E. Electronic structure theory of weakly interacting bilayers. *Phys. Rev. B* **93**, 235153 (2016).
42. Carr, S., Fang, S., Jarillo-Herrero, P. & Kaxiras, E. Pressure dependence of the magic twist angle in graphene superlattices. *Phys. Rev. B* **98**, 085144 (2018).
43. Massatt, D., Carr, S., Luskin, M. & Ortner, C. Incommensurate heterostructures in momentum space. *Multiscale Model. Simul.* **16**, 429–451 (2018).
44. Lehmann, G. & Taut, M. On the numerical calculation of the density of states and related properties. *Phys. Status Solidi b* **54**, 469–477 (1972).
45. Carr, S. et al. Relaxation and domain formation in incommensurate two-dimensional heterostructures. *Phys. Rev. B* **98**, 224102 (2018).
46. Zhou, S., Han, J., Dai, S., Sun, J. & Srolovitz, D. J. van der Waals bilayer energetics: Generalized stacking-fault energy of graphene, boron nitride, and graphene/boron nitride bilayers. *Phys. Rev. B* **92**, 155438 (2015).
47. Wang, L. et al. One-dimensional electrical contact to a two-dimensional material. *Science* **342**, 614–617 (2013).